

# Cryomicroscopy reveals the structural basis for a flexible hinge motion in the immunoglobulin M pentamer

Received: 17 December 2021

Accepted: 12 October 2022

Published online: 23 October 2022

 Check for updatesQu Chen<sup>1</sup>, Rajesh Menon<sup>2</sup>, Lesley J. Calder<sup>3</sup>, Pavel Tolar<sup>2,4</sup> ✉ & Peter B. Rosenthal<sup>3</sup> ✉

Immunoglobulin M (IgM) is the most ancient of the five isotypes of immunoglobulin (Ig) molecules and serves as the first line of defence against pathogens. Here, we use cryo-EM to image the structure of the human full-length IgM pentamer, revealing antigen binding domains flexibly attached to the asymmetric and rigid core formed by the C $\mu$ 4 and C $\mu$ 3 constant regions and the J-chain. A hinge is located at the C $\mu$ 3/C $\mu$ 2 domain interface, allowing Fabs and C $\mu$ 2 to pivot as a unit both in-plane and out-of-plane. This motion is different from that observed in IgG and IgA, where the two Fab arms are able to swing independently. A biased orientation of one pair of Fab arms results from asymmetry in the constant domain (C $\mu$ 3) at the IgM subunit interacting most extensively with the J-chain. This may influence the multi-valent binding to surface-associated antigens and complement pathway activation. By comparison, the structure of the Fc fragment in the IgM monomer is similar to that of the pentamer, but is more dynamic in the C $\mu$ 4 domain.

Natural immunoglobulin M (IgM) assembles into monomers (composed of two heavy and two light chains), pentamers and hexamers. Monomeric IgM serves as a membrane-associated antigen-recognition receptor on the surface of B lymphocytes<sup>1</sup>. Pentameric IgM is secreted into serum, or transported across epithelial cells by the polymeric immunoglobulin receptor (pIgR)<sup>2,3</sup>. IgM hexamers have also been found in the serum, but account for less than 5% of total IgM<sup>4</sup>. An IgM pentamer is over 900 kDa, consisting of ten heavy ( $\mu$ ) chains, each of which has a C-terminal tailpiece which holds them together, ten light ( $\lambda$  or  $\kappa$ ) chains and a joining (J) chain, a 15 kDa polypeptide with no homology to other proteins, which sterically interrupts the addition of a sixth heavy crystal fragment (Fc $\mu$ ) unit<sup>5–7</sup>. As the very first antibody produced after pathogen invasion, the multivalent nature of polymeric IgM molecules gives them remarkable ability to agglutinate particulate antigens in serum<sup>8–10</sup>.

Efforts have been made for decades to study the structure of IgM but have been hindered by its size and flexibility. Individual C $\mu$ 4, C $\mu$ 3,

C $\mu$ 2 and Fab domains have been resolved by X-ray crystallography and NMR<sup>11–17</sup>, complexes of IgM with complement components C1 and C4b have been studied at low resolution by electron cryotomography<sup>18</sup>, and two recent publications revealed the atomic structure of the asymmetric pentameric C $\mu$ 4–C $\mu$ 3 core by single-particle cryo-EM<sup>19,20</sup>. Nevertheless, important questions such as how the peripheral domains are positioned and move with respect to the Fc $\mu$  core remain to be answered, which can only be achieved by imaging the structure of FL-IgM as a whole. Traditionally, structures of the hinge regions of immunoglobulin molecules have been identified by enzymatic fragmentations and sequence homology, according to which IgG and IgA are classified into several subclasses<sup>21–23</sup>. However, little sequence similarity has been found at the hinge-equivalent region of IgM owing to the substitution of an additional Fc domain C $\mu$ 2, which has led to the conclusion that IgM lacks a hinge region<sup>24,25</sup>. This does not necessarily imply that IgM lacks flexibility at this region, and the two potential origins of flexibility are the interdomain regions between C $\mu$ 1 and C $\mu$ 2,

<sup>1</sup>Structural Biology Science Technology Platform, The Francis Crick Institute, 1 Midland Road, London NW1 1AT, UK. <sup>2</sup>Immune Receptor Activation Laboratory, The Francis Crick Institute, 1 Midland Road, London NW1 1AT, UK. <sup>3</sup>Structural Biology of Cells and Viruses Laboratory, The Francis Crick Institute, 1 Midland Road, London NW1 1AT, UK. <sup>4</sup>Institute of Immunity and Transplantation, University College London, Rowland Hill Street, London NW3 2PP, UK.

✉ e-mail: [p.tolar@ucl.ac.uk](mailto:p.tolar@ucl.ac.uk); [Peter.Rosenthal@crick.ac.uk](mailto:Peter.Rosenthal@crick.ac.uk)

and between C $\mu$ 2 and C $\mu$ 3. Evidence of flexibility between the Fc and Fab fragments of IgM have been shown in several studies, where projections of IgM alone or ligand-bound forms were captured in negative stain EM images<sup>7,26,27</sup>. However, where exactly the flexibility comes from, whether at the N- or C-terminus of the C $\mu$ 2 domain or both is still ambiguous.

In this study, we have addressed these questions by analysing the 3D structure of human FL-IgM using a single particle cryo-EM approach, placing the emphasis on understanding the hinge structure and flexibility of IgM. The pentameric core serves as a high molecular weight scaffold to study the structure of the flexibly-attached Fab regions. We resolve an F(ab')<sub>2</sub> at one position of the pentamer, which is stabilised with respect to the core, and interpret disordered density distributions at other Fab positions in terms of a hinge-equivalent motion of IgM. In comparison, we study the structure of the IgM Fc monomer by both cryo-EM and time-resolved single-molecule fluorescence resonance energy transfer (smFRET). We show that while the structure of the monomer is similar to that of the pentameric core, its C $\mu$ 4 domains undergo dynamic separation, which may be relevant to IgM function as the membrane-bound B cell receptor.

## Results and discussion

### Cryo-EM Imaging of full-length IgM Pentamers

Maps of full-length IgM (FL-IgM) obtained by cryo-EM (workflow in Supplementary Fig. 1) show a rigidly assembled core and flexible Fabs at peripheral regions of each subunit. The core, including C $\mu$ 3, C $\mu$ 4, tailpiece and J-chain segments (Fig. 1a), is highly similar to the previously published cryo-EM structure of the IgM core (Supplementary Fig. 1d and Supplementary Fig. 2)<sup>19</sup>, despite the absence of the secretory component (SC) chain in our sample, indicating that the core is

largely stabilised by the tailpiece and J-chain. Similarly, dimeric IgA with and without SC have been found to have relatively small structural differences<sup>28</sup>.

The local resolution decreases radially within the cryo-EM map, indicating that the flexibility increases from the core to peripheral regions of IgM molecule. As with the previously published core structure, our maps show that C $\mu$ 3 has higher degrees of freedom than C $\mu$ 4<sup>19,20</sup>, and our map further reveals the highly flexible C $\mu$ 2 and Fabs. To our surprise, not all C $\mu$ 2s are equally flexible: the C $\mu$ 2-1 domain in subunit 1 has very limited flexibility, confirmed by the additional densities extending from the C $\mu$ 3-1A domain in Fig. 1a. The two subunits within the C $\mu$ 2-1 dimer are clearly identifiable in the map, which is not the case for the other four C $\mu$ 2s viewed at the same threshold level.

Densities at the flexible domains are visible at a lower map contour level (Fig. 1b). Ellipsoid-shaped densities corresponding to the C $\mu$ 2 domains in subunits 2–5 are identifiable (black arrow heads in Fig. 1b), as well as the two Fab arms in subunit 1 (Fab-1/Fab'-1). The map densities of these areas are spherical shapes, indicating that the densities are the sum of several continuous conformations. The densities of Fab/Fab' in subunits 2–5 appear when further lowering the threshold level of the map (Fig. 1c), revealing more conformational flexibility. The densities can be regarded as 3-D probability distributions for the Fab positions. Figure 1d is a cross section through the middle of the map (black dotted line in Fig. 1c) revealing features from the core to the Fab.

Within the IgM pentamer, the unique rigidity of F(ab')<sub>2</sub> in subunit 1 is correlated to the interaction between J-chain and C $\mu$ 3-1A domain. Previously, Li et al.<sup>19</sup> observed that the C-terminal loop in the J-chain (hairpin-3 in Fig. 2a, b) extends towards and forms hydrophobic contacts with C $\mu$ 3-1A domain. In addition, there is no neighbouring C $\mu$ 3 domain to form an interchain disulfide bond at C414, leading to a

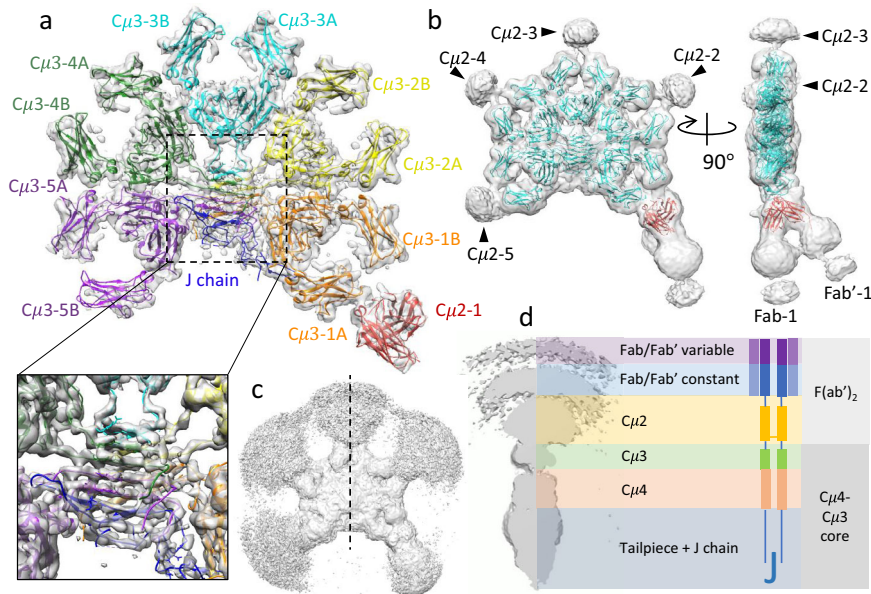


**Fig. 1 | The cryo-EM structure of FL-IgM.** **a** Sharpened cryo-EM map of FL-IgM showing the high-resolution core structure (threshold 0.6). Global resolution 4.3 Å. The model docked in C $\mu$ 4-C $\mu$ 3 areas is IgM core model (pdb id 6KXS, with the secretory component (SC) domain removed) with a unique colour assigned for each subunit (subunit 1, orange; subunit 2, yellow; subunit 3, cyan; subunit 4, green; subunit 5, purple). The model docked in the C $\mu$ 2 domain of subunit 1 is the X-ray model of mouse C $\mu$ 2 dimer (red, pdb id 4JVU). The inset is the zoom-in view of the tailpiece and J-chain region, where individual beta-strands are resolved (local resolution 3.5 Å, see maps for tailpiece and J-chain segments in Supplementary Fig. 2). The resolution of the map decreases along the radial directions from the centre, with 4–5 Å resolution at the C $\mu$ 4 domains and 5.5–7.5 Å at the C $\mu$ 3 domains

for all the ten copies of the IgM Fc core (except for C $\mu$ 3-5B, which is about 1 Å resolution lower than the other C $\mu$ 3s). C $\mu$ 2 in subunit 1 reaches an intermediate-resolution level (6–8 Å). The map coloured with local resolutions is shown in Supplementary Fig. 1g. **b** Unsharpened cryo-EM map of FL-IgM with the threshold set at 0.18 with the same models docked as in (a) (cyan, 6KXS; red, C $\mu$ 2). The densities corresponding to C $\mu$ 2 domains in subunit 2–5 are indicated by black arrowheads. Densities of the two Fab arms are identifiable in subunit 1 (Fab-1 and Fab'-1). **c** The same map as (b) at threshold level 0.025. **d** Half of the cross-section of the map in (c) at the black dotted line in (c), with a schematic of FL-IgM (one subunit) as well as notation given for each component domain.

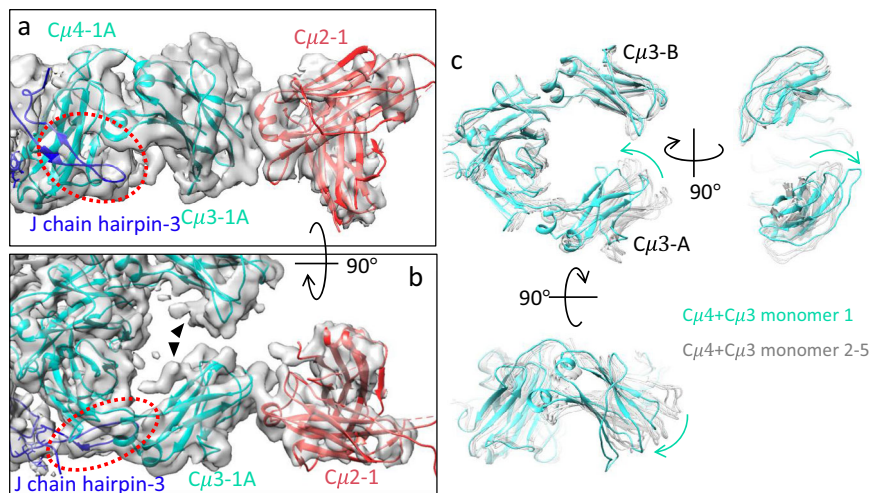


**Fig. 2 | Stabilisation of C $\mu$ 2 domain in subunit 1. a, b** Zoomed-in view at threshold 0.6 of C $\mu$ 2-1 (red, pdb id 4JVU), C $\mu$ 3-1A - C $\mu$ 4-1A (cyan, pdb id 6KXS) and hairpin-3 of J-chain (dark blue) showing the relationships between the domains. The red dotted ellipse highlighting the interacting sections between J-chain and C $\mu$ 3-1A. The black arrowheads in (b) point at the densities corresponding to N-linked

glycosylation at N402 and N395 (densities of glycosylation are visible at all the other C $\mu$ 3 densities in Fig. 1a). **c** Overlay of the C $\mu$ 4-C $\mu$ 3 models of subunit 1 (cyan) and the rest of the subunits (subunit 2-5, light grey). The cyan arrows indicate the relative displacement of C $\mu$ 3-1A.

distinct orientation of C $\mu$ 3-1A compared to the other interlocking C $\mu$ 3 domains. Superimposing C $\mu$ 3 and C $\mu$ 4 domains in subunits 1 and 2-5 (Fig. 2c) reveals that C $\mu$ 3-1A (cyan) is bent both more inward and out-of-plane compared to the other C $\mu$ 3-A domains.

In contrast to the highly flexible C $\mu$ 2 domains which are symmetrically associated with the two adjacent C $\mu$ 3 domains in subunits 2-5 (Fig. 1b), C $\mu$ 2-1 is docked and leaning towards C $\mu$ 3-1A, positioning the short  $\alpha$ -helix (S308-N314) of C $\mu$ 2 near the tip of C $\mu$ 3-1A (T429-P436) which may contribute to the stabilisation of C $\mu$ 2-1 (Fig. 2a-b), though higher resolution data are required to identify detailed side chain interactions. In the model, the straight distances from the C-termini of C $\mu$ 2-1 (C337) to the N-termini of C $\mu$ 3-1A and C $\mu$ 3-1B (I345) are 21 Å and 19 Å respectively (Supplementary Fig. 3a), both of which are much shorter than and therefore compatible with the fully extended linker lengths of eight residues at 3.5 Å per residue. The same stabilization of C $\mu$ 2 and Fab does not occur at subunit 5 on the other side of the molecule, which may be a consequence of the weaker interaction between the J-chain and C $\mu$ 3-5B<sup>29</sup>.

### Structure/conformations of antigen binding F(ab')<sub>2</sub> in subunits

In order to resolve distinct conformations within our cryo-EM map, we conducted 3D variability analysis<sup>30</sup> which reveals the F(ab')<sub>2</sub>, which includes both Fabs and C $\mu$ 2 domains, moves as a rigid body and is able to pivot at the C $\mu$ 2/C $\mu$ 3 interface. Five conformations have been classified from the full dataset (Supplementary Fig. 4), with conformation 4 (pink) displayed in Fig. 3a (the other four maps in Supplementary Fig. 5). While the C $\mu$ 4-C $\mu$ 3 core structures look almost identical among the five classes, they are distinguishable by different orientations of F(ab')<sub>2</sub> in subunit 1. Focused refinement on subunit 1 (dotted box region in Fig. 3a) better resolves the structure of Fab domains, which are shown in Fig. 3b, c (the other four conformations in Supplementary Fig. 5). The two subunits of the constant domain of the Fab (C $\mu$ 1 and CL), as well as the elbows connecting the constant and variable domains, fit well at the domain level between the map and the crystal model pdb id, 2AGJ<sup>31</sup> for all the Fab domains (except for Fab in conformation 2 in Supplementary Fig. 5b, where the density of the variable domain is weaker). Figure 3d illustrates the arrangement of the heavy chains and light chains of F(ab')<sub>2</sub> adopted by the five conformations, where the two inner chains are light chains, and the outer chains, more proximal to C $\mu$ 2, are heavy chains. This arrangement has

slightly better agreement than the configuration with each Fab rotated 180° about its approximate two-fold axis (i.e., heavy chain inside, light chain outside), in fitting the oligosaccharide at N165 (black arrowhead in Fig. 3c). The defined conformation of Fab/Fab' suggests a stabilised association between C $\mu$ 2 and the Fab constant domain.

Superimposing the models for five configurations aligned at the C $\mu$ 4-C $\mu$ 3 core region shows the different orientations of F(ab')<sub>2</sub> (Fig. 3e), revealing that the pivot point for F(ab')<sub>2</sub> (red dots in Fig. 3e) is at the C $\mu$ 2/C $\mu$ 3 interface. Supplementary Movie 1 (front view) and Supplementary Movie 2 (side view) display the flexibility as continuous movements, where F(ab')<sub>2</sub> pivots at the C $\mu$ 2/C $\mu$ 3 interface along both parallel and normal directions to the C $\mu$ 4-C $\mu$ 3 core. No translational movement or rotation about the two-fold symmetry axis of F(ab')<sub>2</sub> is present. The orientations of F(ab')<sub>2</sub> are summarised in Fig. 3f (definitions and measurements are described in the figure legend). The range of in-plane angle  $\alpha$  is between -20° to -45° (same as measured for either Fab and Fab'), and the range of out-of-plane angle  $\beta$  is from -10° to 0° for Fab-1, and -40° to -55° for Fab'-1. The relative angle between the two Fab arms is a constant about 50°, and superimposing the five F(ab')<sub>2</sub> structures shows that they share an identical conformation (Fig. 3g) and indicate a rigid F(ab')<sub>2</sub> structure in subunit 1 of the IgM molecule.

The rigidity of IgM F(ab')<sub>2</sub> is supported by a previous study, where a pair-wise surface binding behaviour was observed in an IgM-surface antigen complex with complement components studied by cryotomography, i.e., both Fab and Fab' are facing towards the binding surface in contrast to only one in IgG (where the other Fab arm is dangling)<sup>18,32</sup>. This behaviour has been observed in all five subunits in the surface-bound IgM and the relative angles between the two Fab arms in the surface-bound IgM are also about 50° to 55°<sup>18</sup>. This supports the idea that the rigidity of F(ab')<sub>2</sub> is intrinsic and universal in all subunits of the IgM molecule. The potential elbow motion between the constant and variable domains in the Fab is small compared to the observed F(ab')<sub>2</sub> flexibility but nevertheless important for antigen binding mechanisms for immunoglobulins<sup>33</sup>. Another phenomenon worth noting is that pentameric IgM is asymmetric with a biased Fab-1/Fab'-1 orientation towards the - $\beta$  side, which is also the side identified by J-chain hairpin-3. The 120° bending of F(ab')<sub>2</sub> observed in the surface-bound IgM<sup>18</sup>, much larger than the 55° (Fig. 3f) in the free-form IgM, indicates that F(ab')<sub>2</sub> of subunit 1 can be highly strained when



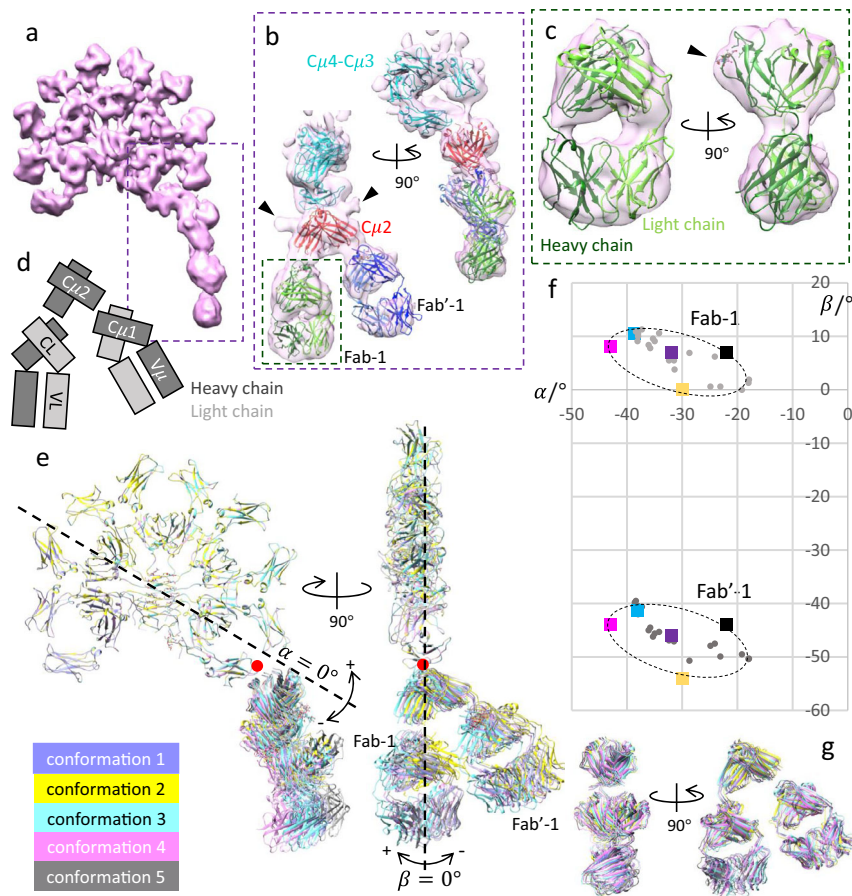


**Fig. 3 | Structure of  $F(ab')_2$  in subunit 1 and its flexibility.** **a** One of five conformations (conformation 4) classified from 3-D variability analysis (3DVA). Threshold of the map is 2.4. **b** Map obtained by focused-refinement of the conformation 4 at subunit 1 (dotted box in **a**). B factor used for map sharpening is  $-400 \text{ \AA}^2$  and the threshold of the map is 2. The two black arrowheads point at the N-linked glycosylation at N332 in  $C\mu 2$  dimer. **c** Zoomed-in view of Fab-1 (green dotted box in **b**), with location of oligosaccharide at N165 on heavy chain indicated by the black arrowhead. Models docked in **(b, c)** are pdb id 6KXS (cyan, subunit 1 only), pdb id 4JVU (red) and two crystal models of IgM Fab (green and blue, pdb id 2AGJ) for Fab-1 and Fab'-1. The heavy chains are dark green/blue and light chains are light green/blue. The maps for the other four conformations and corresponding focused refined maps are in Supplementary Fig. 5. **d** Schematic of the heavy and light chain arrangement in  $F(ab')_2$ . **e** Overlay of the models of five

maps with different  $F(ab')_2$  conformations aligned at their common  $C\mu 4$ - $C\mu 3$  core region. The in-plane ( $\alpha$ ) and out-of-plane ( $\beta$ ) and the positive/negative axes of  $F(ab')_2$  are defined. The orientation of each Fab/Fab' arm is defined as the direction from the C-terminus of  $C\mu 2$ -1 to the centre of the constant domain  $\alpha = 0^\circ$  is defined as the two-fold symmetry axis of  $C\mu 4$ -1 A/1B dimer, and  $\beta = 0^\circ$  is the platform formed by  $C\mu 4$ - $C\mu 3$  core (black dotted lines).  $\alpha$  and  $\beta$  are the relative angles between Fab/Fab' and  $\alpha = 0^\circ/\beta = 0^\circ$ . **f** Summary of  $\alpha$  and  $\beta$  in the five conformations. The datapoints are the same colours as the maps in **(e)**. The grey datapoints are the Fab/Fab' values measured from the 20 frames in the volume series calculated by 3DVA showing the continuous flexibility of  $F(ab')_2$  in subunit 1 (Supplementary Movie 1 and Supplementary Movie 2). **g** Superimposition of the  $F(ab')_2$  structures in all five conformations.

binding to surface antigens. It cannot be achieved by simply extending the pivot motion to  $120^\circ$  because the  $C\mu 2$ -1 and  $C\mu 3$ -1 A domain would clash, instead requiring an extension of the linker between  $C\mu 2$  and  $C\mu 3$  domain to accommodate the extreme bending angle of  $F(ab')_2$ . The intrinsic asymmetry of the free IgM suggests that it is more energetically favourable for IgM to engage surface antigens using the  $-\beta$  side, predisposing the  $+\beta$  side to engage with the C1q molecule of complement<sup>34</sup>. The C1q binding site on  $C\mu 3$ -1 may be identified by superimposing the IgM conformations and IgG-Fc/C1q complex model (pdb id 6FCZ<sup>32</sup>), which reveals steric clashes between  $C\mu 2$ -1 and C1q. Therefore, the C1q binding site on  $C\mu 3$ -1 may be inaccessible for C1q binding until  $C\mu 2$ -1 is displaced, such as when IgM binds to surface antigens.

IgM is widely described as lacking a hinge region, which is replaced by a whole Fc domain  $C\mu 2$ <sup>34</sup>. A typical hinge in an immunoglobulin molecule such as IgG or IgA usually consists of three parts – an upper hinge at the  $C_H1$  C-terminus, a core hinge composed of

multiple prolines and cysteines, and a lower hinge at the N-terminus of  $C_H2$  domain. The lower hinge allows the movement of the two Fab arms relative to the Fc domains, while the upper hinge provides independent freedom for each Fab, as demonstrated in previously published studies of IgG and IgA<sup>28,35,36</sup>. The hinge-equivalent region in IgM is  $C\mu 2$  as well as its two junctions at the N- and C-termini.  $C\mu 2$  itself is a rigid dimer linked by a disulfide bond, which spatially separates Fabs from the  $C\mu 4$ - $C\mu 3$  core as a core hinge does in IgGs and IgAs<sup>21</sup>. The N-termini of  $C\mu 2$  with the proline-rich linker region seem not to be able to provide motions (very little if any) for each Fab arm, as suggested by the observation of the rigid V-shaped  $F(ab')_2$  configuration in subunit 1 of IgM. The C-termini of  $C\mu 2$  are flexible which resembles a classic lower hinge<sup>37</sup>, allowing the  $F(ab')_2$  to move relative to the core. However, the range of freedom is limited by its short length which explains why the flexibility of  $F(ab')_2$  in subunit 1 is analogous to pivoting instead of more complicated behaviours.

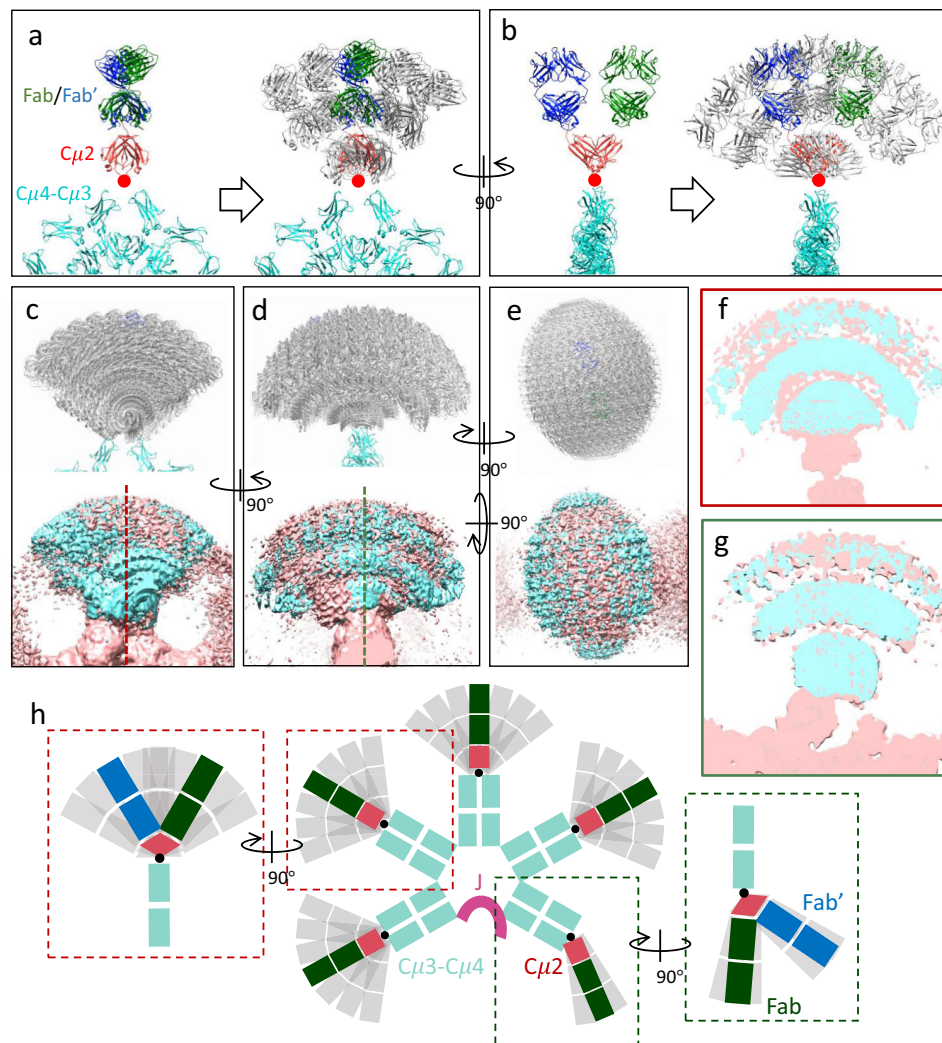


**Fig. 4 | Model-based interpretation of the density of F(ab')<sub>2</sub> in subunit 2-5 based on the structure and flexibility of F(ab')<sub>2</sub> in subunit 1.** **a** F(ab')<sub>2</sub> model rigidly translated from subunit 1 to subunit 4 (left panel), and in-plane pivoting of F(ab')<sub>2</sub> at the C $\mu$ 2/C $\mu$ 3 interface (right panel). **b** Left panel, side view of the left panel in (a). Right panel, out-of-plane pivoting of F(ab')<sub>2</sub> at C $\mu$ 2/C $\mu$ 3 interface. Red dots in (a, b) are the pivot point. **c-e** Upper panel, array of F(ab')<sub>2</sub> models with the in-plane and out-of-plane ranges of C $\mu$ 2 rotation at both  $\pm 50^\circ$  with  $10^\circ$  interval. The actual in-

plane and out-of-plane directions are slightly tilted to match the tilted two-fold axes of the F(ab')<sub>2</sub> density (shown in Supplementary Fig. 6a–c). Lower panels, overlay of the experimental (pink) and simulated map (cyan) of F(ab')<sub>2</sub>. Threshold level of the map is 0.025. **(f, g)** Cross-sections of the overlaid maps indicated by the dotted lines in (c) and (d). **h** Illustration of the overall structure of FL-IgM showing the two levels of flexibilities of F(ab')<sub>2</sub> among the five subunits.

The reconstructed map is the convolution of the map density of the molecule with the functions that describe the motions, so knowing the structure of F(ab')<sub>2</sub> and the pivot motion in subunit 1 explains the density distributions in subunit 2-5. Pivoting the C $\mu$ 2 model by  $\pm 50^\circ$  along both the in-plane and out-of-plane directions gives a good agreement with the shape of the map density (Supplementary Fig. 6a and Supplementary Fig. 6b), and the two symmetry axes of the density are tilted about  $10^\circ$  anti-clockwise from the C $\mu$ 4-C $\mu$ 3 platform (Supplementary Fig. 6c). When the pivoting motion is applied to the whole F(ab')<sub>2</sub>, one can see a good agreement between simulated data and experimental data (Fig. 4a to 4g, Supplementary Fig. 7), which implies that the motion of F(ab')<sub>2</sub> we propose here can explain the cryo-EM map densities reasonably well and F(ab')<sub>2</sub> can indeed bend to much larger angles when not stabilised by the J-chain. Because of the  $50^\circ$  splaying of the two Fab arms in the out-of-plane direction (Fig. 3e, f), the map density range along the out-of-plane direction appears larger by about  $25^\circ$ , roughly half the angle between the two Fab arms. This is confirmed by quantitatively analysing the map densities (method and calculations in 'Quantification of the

range of Fab motion in subunit 2-5' in Methods and Supplementary Fig. 8 and Supplementary Fig. 9). For all four subunits 2-5, the map density range along the in-plane direction is in the range of  $\pm 50^\circ$ – $60^\circ$  (Supplementary Fig. 9c and Supplementary Fig. 9e) while the range along the out-of-plane direction is about  $\pm 70^\circ$ – $80^\circ$  (Supplementary Fig. 9d and Supplementary Fig. 9f). This agrees well with the  $\pm 50^\circ$  motion range along both in-plane and out-of-plane directions estimated from the model-based interpretation. When binding to surface antigens, an additional  $40^\circ$ – $50^\circ$  bending is required to accommodate the 'staple-form' IgM as well as expose the C1q binding sites<sup>18</sup>, possibly accompanied by some degree of linker extension similarly to subunit 1.

### Structure and dynamics of the IgM monomer

We have also studied the IgM-Fc monomer (defined as C $\mu$ 4-C $\mu$ 3-C $\mu$ 2 dimer) by both smFRET and cryo-EM for comparison to Fc in the pentamer. Two potential C $\mu$ 4 arrangements of the IgM-Fc monomer have been reported: one is the 'parallel' conformation proposed by Müller et al (pdb id 4JVW)<sup>11</sup>, while the other is 'anti-parallel', which

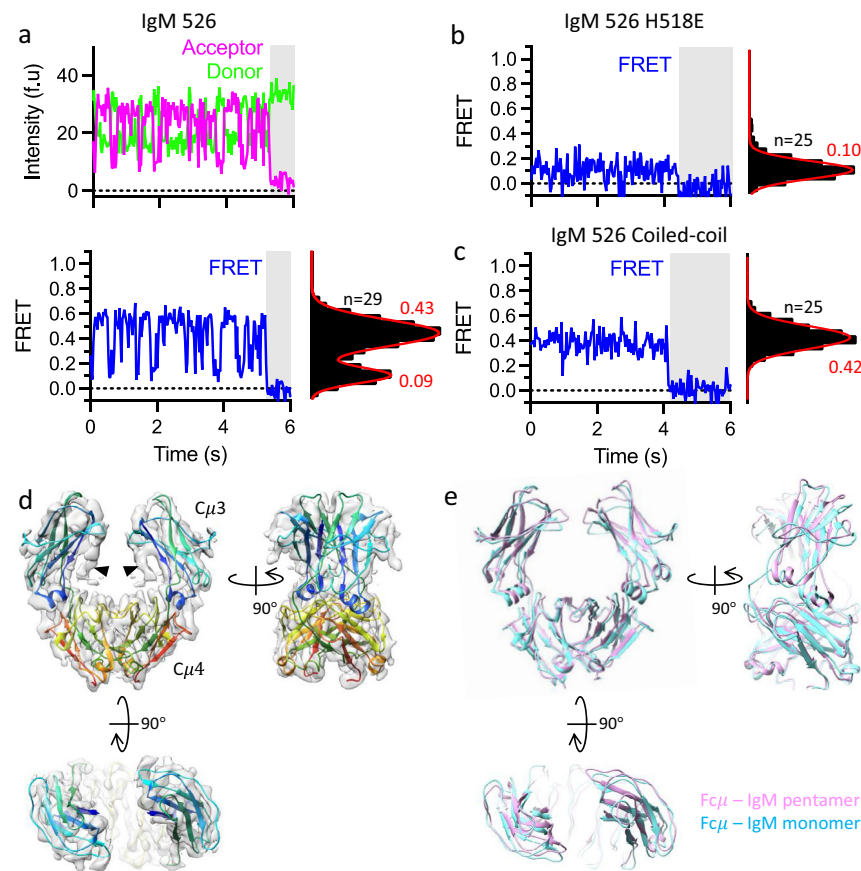


**Fig. 5 | Dynamics of the IgM monomer based on smFRET and cryo-EM structure comparisons.** **a** FRET donor (green) and acceptor (magenta) fluorescence intensity traces and the calculated FRET efficiency (blue) from a single molecule of a monomeric IgM-Fc construct labelled with the fluorophores at position 526 in the EF helix of C $\mu$ 4. The shaded area indicates when the acceptor molecule is photo-bleached. The histogram along the right FRET axis shows the distribution of the single-molecule FRET values for the  $n$  molecules measured. **b, c** Examples of single-molecule FRET traces and the respective distribution of FRET values for monomeric IgM-Fc constructs labelled at position 526 and containing either a mutation H518,

which disrupts C $\mu$ 4 dimerization (**b**) or C-terminal coiled-coil, which forms a stable dimer (**c**). **d** Cryo-EM structure of IgM-Fc monomer with C-terminal coiled-coil showing the two-fold symmetrical arrangement at C $\mu$ 4 and C $\mu$ 3 regions (threshold 0.47). Black arrowheads indicate the density corresponding to the N-linked glycosylation at N395. **e** Superimposing the models of monomeric and a pentameric subunit (subunit 4 in pdb 6KXS) IgM showing similarity of the two structures, with slight variations at the orientations of C $\mu$ 3 domains. Source data are provided as a Source Data file.

resembles the subunits in the IgM pentamer and the C-terminal domains of other Ig molecules such as IgG<sup>38</sup>, IgA<sup>39</sup> and IgE<sup>40</sup> (Supplementary Fig. 10a–c). Intriguingly, our time-resolved smFRET (Supplementary Fig. 10d, e) at two different labelling positions (Supplementary Fig. 10a, b) showed that the C $\mu$ 4 dimer in the IgM monomer is dynamic, yielding two discrete FRET states, which interchange several times per second (Fig. 5a, and Supplementary Fig. 11a). A comparison of the experimentally measured distances of the two labelled residues to the predicted distances calculated from the ‘parallel’ and ‘anti-parallel’ conformations (Supplementary Fig. 10a, b, Supplementary Table 1) reveals that the high FRET states (‘closed’ conformation) agree with the ‘anti-parallel’ conformation found in pentameric IgM, while the low FRET states (‘open’ conformation) do not align with either of the conformations. In contrast, the IgG Fc produced only one FRET state, which agreed with the distances calculated from the crystal structure (Supplementary Fig. 10c, Supplementary Fig. 11b, c, and Supplementary Table 1). This is consistent with C $\gamma$ 3 forming a stable dimer<sup>41</sup>, as is the case for C $\epsilon$ 4<sup>42</sup>, but unlike C $\mu$ 4. We then modified the C $\mu$ 4–C $\mu$ 4 interactions and captured the ‘closed’ and ‘open’ conformations of IgM Fc separately. Mutation of the histidine at the centre of the C $\mu$ 4 dimer interface (H518E) disrupting dimerization produced a single low FRET state (‘open’ conformation, Fig. 5b), whereas stabilisation of the

C-terminus by a coiled-coil domain produced a single FRET state corresponding to the high FRET state of the wild-type construct (‘closed’ conformation, Fig. 5c).

This observation indicates that the C $\mu$ 4 dimer in the IgM monomer is inherently dynamic and is stabilised by external interactions. In the IgM pentamer, it is achieved by the tailpieces<sup>43</sup>, neighbouring IgM subunits and the J-chain. For the monomeric IgM expressed on membrane, given that the stalk that connects the IgM monomer to the cell membrane lacks a stabilising disulfide bond that is present in IgG, IgA and IgE, stability can be potentially provided by the transmembrane helices or by interactions with the Ig $\alpha$  and Ig $\beta$  subunits. Therefore, the unique dynamics at the IgM C $\mu$ 4 domains may play a role in isotype-specific assembly of the membrane IgM into the B cell receptor complex or its function after antigen binding.

The cryo-EM structure of IgM-Fc stabilised by the coiled-coil domain further confirms the resemblance between the ‘closed’ conformation of the IgM-Fc monomer to the subunits among subunit 2–5 in the IgM pentamer (workflow in Supplementary Fig. 12). Figure 5d illustrates the IgM-Fc model aligned with the cryo-EM map and superimposing the C $\mu$ 3–C $\mu$ 4 backbone models of the F $\mu$  monomer and subunit 4 of the IgM pentamer shows a good match at C $\mu$ 4 dimer with RMSD = 0.72 Å, whereas subtle mismatch occurs at C $\mu$ 3 domains, where the C $\mu$ 3 in monomeric F $\mu$  is slightly closer to C $\mu$ 4 (Fig. 5e). The



differences in the C $\mu$ 3 domains are in line with a stabilising effect of the interdomain disulfide bond at C414 in the IgM pentamer. The symmetrical structure of the IgM-Fc monomer also supports the idea that the asymmetry observed at subunit 1 in the IgM pentamer is attributed to the interaction with the J-chain.

By cryo-EM imaging, we have shown an asymmetric and flexible full-length IgM pentamer. The features of the structure are summarised in Fig. 4h. Our results show that the IgM core, including C $\mu$ 4, C $\mu$ 3 and J-chain, adopts a structure superimposable with that previously described<sup>19,20</sup> also in the absence of the secretory component, consistent with the role of the secretory component in transport rather than signalling. We have found different flexibilities at the Fab domains compared to IgGs and IgAs, owing to its unique hinge-equivalent structure at the interface between the C $\mu$ 3 and C $\mu$ 2 domains. Our understanding of IgM motions may be applicable to IgE, which lacks the hinge region typical of IgG and IgA, but likely contains a similar hinge-equivalent region to IgM based on sequence comparison. Previous analysis of IgE structure suggests that IgE Ce2 can undergo a similar motion as we have observed for IgM. A crystal structure of IgE-Fc shows a Ce2 domain acutely bent to one side of the Fce interacting with Ce3-Ce4<sup>40</sup>, whereas a symmetric complex of IgE-Fc with antibody fragments stabilises Ce2 in an extended position<sup>44</sup>. A cryo-EM structure of an IgE:FceRI complex with antibody fragments also shows Ce2 can adopt an extended position<sup>45</sup>.

The observed asymmetry of the IgM pentamer originates from the J-chain, which extends to and interacts with the C $\mu$ 3-1A domain, leading to the stabilisation of C $\mu$ 2 and Fab domains. The complement cascade starts from concerted antigen engagement by IgM which exposes C1q binding sites on C $\mu$ 3 domains. IgM F(ab')<sub>2</sub> is likely to be strained during multivalent binding of surface antigens. Interestingly, the IgM hexamer has been reported to be at least several-fold more potent in deposition of complement than the IgM pentamer<sup>4,46,47</sup>. Because the difference is large and found to be more pronounced at low antigen concentrations<sup>46</sup>, it is likely the result of the way the Fabs can interact with antigen and expose C1q binding sites. The asymmetric behaviour of F(ab')<sub>2</sub> of subunit 1, which is indirectly stabilised by the J-chain and blocks the C1q binding site, could contribute to this difference in fully symmetric complement deposition from the IgM hexamer without the J-chain<sup>18</sup>. This suggests an important effect for the asymmetric behaviour of the Fabs in complement activation.

During the revision of this work, IgM-BCR structures were published by two independent groups<sup>48,49</sup>. Though the Fab regions display some flexibility, these structures show the C $\mu$ 2 and Fab domains in similar positions to those of the stabilised C $\mu$ 2 and Fab in the IgM pentamer subunit 1 (Supplementary Fig. 13a). It is striking that in both cases the stabilisation of C $\mu$ 2 results from a similar, asymmetric C $\mu$ 3 Fc region (Supplementary Fig. 13b), where one C $\mu$ 3 domain is displaced compared to the symmetric subunits of the IgM pentamer or the symmetric IgM Fc monomer (Supplementary Fig. 13c, d). While in the case of pentameric IgM this asymmetry may be attributed to interactions with the J-chain, in the IgM-BCR the C $\mu$ 3 asymmetry arises from the interaction of one C $\mu$ 3 domain with the Ig $\alpha$  chain. It is reasonable to speculate that in the BCR, C $\mu$ 3 asymmetry may couple the Fab domain to membrane components involved in B-cell signalling and that this may involve mechanisms that are conserved in secreted pentameric IgM.

We have also shown that the C $\mu$ 4 domains in the IgM monomer are inherently dynamic, but are stabilised by a coiled-coil which may mimic the transmembrane segments. Coiled-coil interactions have now been visualised in the transmembrane region of the IgM-BCR structures. Furthermore, the topological complexity of the membrane proximal region may be consistent with a requirement for co-assembly of IgM and Ig $\alpha\beta$  to form the IgM-BCR<sup>48,49</sup>. Given that the membrane

IgM is unique in lacking a disulphide bond in the stalk, a dynamic separation of the C $\mu$ 4 domains may help regulate the assembly of IgM with Ig $\alpha\beta$  to form the IgM-BCR complex in an isotype-specific manner, or regulate activation of the IgM BCR after antigen binding.

Overall, our findings on the structure and flexibility of the pentamer and monomer instruct IgM hinge engineering for therapeutic and diagnostic applications<sup>50-52</sup>.

## Methods

### Protein expression and purification

Full-length IgM pentamer. Human IgM pentamer from myeloma (Jackson ImmunoResearch, RRID: AB\_2337048) was purified using a Superose 6 10/300 GL column to remove trace amounts of dimers and hexamers. The protein was concentrated at 1.0 mg/ml in PBS.

IgM-Fc monomer and IgG1-Fc. Recombinant human IgM-Fc and IgG1-Fc were based on the extracellular parts of the membrane forms of the immunoglobulins. The IgM Fc monomer contained C $\mu$ 2-C $\mu$ 4 domains followed by the stalk normally linking the extracellular domains to the transmembrane region (residues 228-569) and included a mutation of C444S to prevent oligomerization and incorporation of fluorescent dyes at this position. IgG1 Fc contained C $\gamma$ 2-C $\gamma$ 3 followed by the stalk (residues 227-464) and included mutation of the hinge cysteine (C229S), which also interfered with labelling. None of the mutations affected the expression, dimerization, or stability of the IgM and IgG1 proteins.

To introduce fluorescent labels at sites whose distances could distinguish the mode of C $\mu$ 4 orientation and dynamics, residues E526 (in the EF helix) and T556 (at the end of the G strand) at the side and bottom of C $\mu$ 4 of IgM, respectively, were mutated to cysteines. Correspondingly, amino acids S415 and S444 in C $\gamma$ 3 of IgG1 were mutated to cysteines. To disrupt C $\mu$ 4 dimerization, histidine at position 518 in the C $\mu$ 4 domain was mutated to glutamic acid. The C $\mu$ 4 dimerization was stabilised by adding a C-terminal self-dimerising coiled-coil (EIAQLEYEISQLEQEIQALES)<sup>53</sup>. These two latter changes were introduced into IgM E526C. All constructs were cloned into pHLSec vector, in a frame with an N-terminal signal peptide sequence for secretion and with a C-terminal twin Strep Tag for purification of the secreted proteins.

The proteins were expressed by transient transfection of the plasmids into adherent 293 T cells using PEI (1.0  $\mu$ g/ $\mu$ l, 1:4 (w/w) DNA to PEI). Transfected cells were cultured for 5 days and the media containing the proteins were collected, filtered and applied to a Strep-Tactin sepharose column (IBA Life Sciences). Bound proteins were eluted with desthiobiotin and purified using FPLC.

### Cryo-EM sample preparation and imaging

Full-length IgM pentamer. Purified IgM pentamer samples were diluted to 0.25 mg/ml and 4  $\mu$ l were applied to amylamine glow-discharged holey carbon copper grids (Quantifoil, R2/2) in the environmental chamber of a Vitrobot Mark IV (FEI/Thermo) at 4 °C and 100% humidity, and the grid was blotted with filter paper and then plunge frozen in liquid ethane at liquid nitrogen temperature. The IgM cryo grids were screened on Talos Arctica microscope (FEI/Thermo) at 200 kV and data collection performed on a Titan Krios microscope (FEI/Thermo) at 300 kV using EPU software. Movies were recorded on a Falcon 3 camera in counting mode with a total dose of 34.2 electrons per  $\text{Å}^2$  fractionated over 30 frames (dose rate 0.51 e<sup>-</sup>/ $\text{Å}^2$ /s) with a 1.09  $\text{Å}$  pixel size and a defocus range between -1 to -5  $\mu$ m.

IgM Fc monomer. Purified IgM Fc monomer (with coiled-coil extension at C-terminus) were diluted to 0.2 mg/ml and cryo-EM grids were made and screened using the same approach as the IgM pentamer above. Data were collected on a Titan Krios microscope (FEI/Thermo) at 300 kV equipped with a Gatan Imaging Filter (GIF) using EPU software. The slit width of the energy filter was set to 20 eV. Movies were recorded on a K2 camera in counting mode with a total

dose of 66 electrons per Å<sup>2</sup> fractionated over 40 frames (dose rate 8.25 e<sup>-</sup>/Å<sup>2</sup>/s) with a 0.839 Å pixel size and a defocus range between -1 to -4 μm.

### Cryo-EM data processing and model docking

Full-length IgM pentamer. The workflow of data processing is shown in Supplementary Fig. 1. A total of 43,530 movies were collected and imported into Scipion (v 2.0) in streaming mode. Raw movies were then aligned and dose-weighted by Motioncor2<sup>54</sup>, followed by CTF estimation by CTFind v 4.1.13 on the dose-weighted micrographs<sup>55</sup>. 1500 particles were manually picked in 50 micrographs acquired at various defocus values for model training by crYOLO<sup>56</sup>, which was then used for picking particles from all the micrographs. A total of 1,819,931 picked particles were extracted and exported by Relion particle extraction and export, with a box size of 600 pixels. The following image processing steps were conducted in CryoSPARC (v 3.2.0)<sup>57</sup>. All raw particles were imported into CryoSPARC and after two rounds of 2D classification, 546,583 particles were selected for further analysis. Five ab initio classes were calculated and used as initial models for heterogeneous refinement. 301,286 particles in the two best classes were then combined and subjected to non-uniform refinement<sup>58</sup>. This resulted in a map with a 4.32 Å global resolution calculated by Phenix<sup>59</sup>. Sharpening with B factor of -197 Å<sup>2</sup> was applied to boost the high-resolution features of the map.

3D variability analysis (3DVA) was conducted to explore the flexibility within the IgM molecule (Supplementary Fig. 4)<sup>30</sup>. The 301,286 particles contributing to the final refined map were downsampled by a factor of 2 (box size = 300 pixels), and three components were calculated. The volume series shown in the Supplementary Movie 1 and Supplementary Movie 2 is the first variability component. At the same time, the particles were clustered into six subsets by 3DVA, five of which were individually reconstructed by non-uniform refinement to improve particle alignments and resolution. Particle subtraction and focused refinement for each class were then calculated to improve the alignment and resolution locally at subunit 1, especially the F(ab')<sub>2</sub> region.

Models (pdb id 6KXS, 4JUV, 2AGJ) were rigidly docked and combined into the maps and geometry minimisation was performed to regularise the models, followed by rigid body refinement using respace refinement in Phenix<sup>59</sup>. The maps and models were displayed in Chimera v 1.13.1<sup>60</sup>. Details on data recording and processing of the FL-IgM pentamer are summarised in Supplementary Table 2.

IgM Fc monomer. 14,815 movies were collected, which were aligned and dose-weighted by Motioncor2 in Relion3.1<sup>61</sup>, followed by CTF estimation by CTFind v 4.1.13. 7,411,324 particles were picked from 13,012 selected micrographs by a trained model in crYOLO and extracted with a box size of 50 pixels (pixel size=3.356 Å). The particle stack was cleaned by 2D classification in CryoSPARC for two rounds, with 961,072 particles selected and re-extracted with a box size of 256 pixels (no binning, pixel size=0.839 Å), which were then processed with Relion for 3D initial model, 3D auto-refine, Bayesian polishing and CTF refinement<sup>61,62</sup>. The polished and CTF-refined particles were transferred back to CryoSPARC for non-uniform refinement with C2 symmetry. The final map has a global resolution of 3.6 Å and a B factor of 185 Å<sup>2</sup>.

Initial model of mIgM-Fc is obtained from chain E and F from the IgM pentamer cryoEM structure (pdb id 6KXS). Tailpieces were removed and single mutation C414S was made on both chains. Real-space refinement of the model against the mIgM-Fc cryo-EM map was then conducted in Phenix (v1.19.2) and manual refinement in Coot (v0.9.6). map-model FSC at 0.5 cut-off is 3.79 Å. The maps and models were displayed in Chimera v 1.13.1<sup>60</sup>. Details on data recording and processing of IgM Fc monomer are summarised in Supplementary Table 3.

### Quantification of the range of Fab motion in subunit 2-5

The whole IgM map is composed of a series of cross-sections along any orientation, as shown in Supplementary Fig. 8a. The cross-sections are opened in ImageJ (v 2.1.0), converted to 8-bit, and filtered with an isotropic 3D Gaussian function with  $\sigma=3$  px to reduce the high-frequency noise which would influence the accuracy for the following measurements.

Supplementary Fig. 8b–e are the middle cross-sections of all the F(ab')<sub>2</sub> clouds along both in-plane and out-of-plane directions, and thus represent the maximum angle that the Fab can reach in each subunit. The curvatures of the inner and outer arc indicate that they share the same centre, which is the hinge region of F(ab')<sub>2</sub> motion at the C-terminus of the C $\mu$ 2 domain. This is confirmed by fitting the centre of each arc into a circle (dashed circles in Supplementary Fig. 8b–e), and the blue spots shown in the cross-sections are the shared centre of the arcs at C $\mu$ 2/C $\mu$ 3 interface.

The Fab motion range can be quantified based on the grey values on the inner (Fab constant region) and outer (Fab variable region) arcs on the cross-sections. One can see from the cross-sections that for either the inner or outer arc the grey value at the centre is the highest (brighter), and it becomes darker with the length of the arc extending both ways and finally falls to the level of the background. Supplementary Fig. 9a and Supplementary Fig. 9b demonstrate the approach to measure the grey values of the arcs in a series of in-plane angle  $\alpha$  and out-of-plane angle  $\beta$  for subunit 4. The line profiles are plotted using the 'plot profile' function in ImageJ<sup>63</sup>. Three peaks are present in the plots, corresponding to the densities of C $\mu$ 2, Fab constant domain (inner arc) and Fab variable domain (outer arc). The values of all three peaks decrease monotonically with  $\alpha$  or  $\beta$  increases, and at some point, the peaks of inner and outer arc are not significantly higher than the background (black curves).

The criteria used in this study for the peak grey value to be considered as above noise is described in Eq. (1)

$$\frac{\text{grey value} - \overline{\text{BKG}}}{\sigma_{\text{BKG}}} \geq 2 \quad (1)$$

where  $\overline{\text{BKG}}$  is the mean of the background noise, and  $\sigma_{\text{BKG}}$  is the standard deviation of the background noise. The  $\alpha$  or  $\beta$  at which the result of the above equation equals 2 is regarded as the boundary of the Fab moving range. Supplementary Fig. 9c to Supplementary Fig. 9f summarises the results for subunit 2-5 along both positive and negative directions. Six data points were collected on six consecutive cross-sections around the middle section for each subunit. These results quantitatively demonstrate that the in-plane flexibilities of Fab is in the range of 50° – 65° and 70° – 80° along the out-of-plane direction, and there is no significant difference among subunit 2-5, or along positive or negative directions.

### Labelling of IgM monomers and IgG1 Fc proteins and smFRET microscopy

The proteins were labelled at the introduced cysteines with FRET pair dyes using Alexa Fluor 555 C2 maleimide and Alexa Fluor 647 C2 maleimide (both from ThermoFisher). Before labelling, proteins were buffer-exchanged into 50 mM Tris (pH 6.8), 140 mM NaCl and 20 μM TCEP. A five times molar excess of each dye, prepared in labelling grade DMF (Lumiprobe), was simultaneously added to the protein and the mixture was incubated with shaking at room temperature for 2 h. Labelled proteins were purified by size exclusion chromatography using a Superdex 200 10/300 GL column. Dye incorporation was examined by SDS-PAGE gels using ImageQuant imaging system (Amersham) and by absorbance measurements. Calculation of dye incorporation generally showed a near 1:1 incorporation of each dye with more than 90% protein labelled. No significant labelling was observed of control proteins lacking the introduced cysteines.



Borosilicate glass coverslips (VWR) were treated with acid piranha solution (a 3:1 mixture of concentrated sulphuric acid with hydrogen peroxide) in glass jars for 15 min. The coverslips were extensively washed with distilled water followed by 2 washes with ethanol and one final wash again with distilled water. Coverslips were then washed three times with acetone to remove all traces of water. The coverslips were then incubated with 2% (v/v) silane (3-aminopropyltriethoxysilane, Sigma) in acetone. After 2 min, coverslips were rinsed thoroughly with distilled water. The coverslips were dried under argon and mounted on microscope slides using two 0.12 mm-thick strips of double-sided adhesive tape (Sigma). The two strips were separated by a gap of about 4 mm creating a channel for the application of the samples.

In order to specifically attach the labelled proteins, the slide-mounted coverslips were first coated with biotin-PEG as follows: 2 mg biotin-PEG SVA and 150 mg of mPEG-SPA (both from Laysan Bio) were dissolved in 1 ml of 0.1 M NaHCO<sub>3</sub> (pH 8.2) and applied to the channels between each coverslip and the slide. The coverslips were left with the coverslip side down in a humidified chamber for 3 h. Afterwards, the channels were washed extensively with distilled water and dried under argon. The coverslips were either immediately used or stored under vacuum in a desiccator for up to 3 weeks. Prior to the experiments, the channels were coated with streptavidin (1.0 mg/ml in PBS) for 30 min. After washing out unbound streptavidin, the channels were loaded with biotinylated anti-IgM or anti-IgG antibodies serving as anchors for the fluorescent proteins. IgM Fc was captured using monoclonal antibodies directed against the C<sub>μ</sub>2 domain of IgM (anti-human IgM MU53 and HBS7, generous gifts from Patricia Mongini<sup>64</sup>, Feinstein Institutes for Medical Research). IgG1 Fc proteins were captured using anti-IgG1 antibodies directed against the C<sub>γ</sub>2 domain (Bio-Rad, anti-human IgG clone MK1A6).

Labelled proteins were applied to channels containing the antibodies at an appropriate dilution to achieve a sparse surface density suitable to imaging of individual fluorescent spots. After washing, PCA/PCD/Trolox oxygen scavenging buffer (0.385 mg/ml Protocatechuic acid, 7 μg/ml Protocatechuate 3,4-dioxygenase, 0.3 mg/ml Trolox (all from Sigma) in Tris-buffer saline pH 8) was introduced for single molecule imaging.

The samples were imaged on an Olympus IX-81 TIRF microscope with iLAS laser illumination system, 100x objective, image splitter and Andor iXon camera (CAIRN imaging). The sample was initially imaged by acquiring a donor image (illumination at 552 nm and emission at 565–615 nm), a FRET image (illumination at 552 nm and emission at >650 nm) and a directly excited acceptor image (illumination at 637 nm and emission at >650 nm), followed by time-lapse imaging at 30 ms per frame using 552 nm excitation and simultaneous imaging of the donor and acceptor (FRET) emission.

### FRET data analysis and dye distance calculation

Single-molecule FRET was analysed similarly as described previously<sup>65,66</sup> using automated image processing in Matlab (Mathworks) and semi-automatic identification of single-molecule fluorescent traces. All imaging channels were spatially aligned using multispectral beads. Background in each channel was subtracted using background images generated by medium filtering at each pixel position across many experimental images containing sparse single-molecule fluorescence spots. Spots containing both donor and acceptor molecules were identified using initial snapshots of the acceptor fluorescence and recovered donor fluorescence, which was calculated as Eq. (2)

$$\text{Recovered donor fluorescence} = D + F/\gamma \quad (2)$$

where D is the donor image intensity (donor excitation and donor emission), F is the FRET image intensity (donor excitation and acceptor

emission) and  $\gamma$  is the factor that relates fluorescence intensity of F to D, measured from donor recovery after acceptor photobleaching of molecules exhibiting non-zero FRET in each experiment as Eq. (3)

$$\gamma = (F_{\text{before}} - F_{\text{after}})/(D_{\text{after}} - D_{\text{before}}) \quad (3)$$

FRET efficiency of individual molecules over time from time-lapse images was calculated as Eq. (4)

$$E = (F - \alpha D - \beta A)/(F - \alpha D - \beta A + \gamma D) \quad (4)$$

where D, F and A are the mean pixel intensities of a 5 × 5 pixel area of the fluorescent spot in the donor, FRET and directly-excited acceptor channels, respectively,  $\alpha$  is the fraction of donor fluorescence bleeding into the FRET channel ( $\alpha = F/D$  in donor-only molecules),  $\beta$  is the fraction of FRET channel fluorescence attributable to direct 552 nm excitation of the acceptor ( $\beta = F/A$  in acceptor-only molecules), and  $\gamma$  is as explained above. The correction factors  $\alpha$ ,  $\beta$  and  $\gamma$  were determined in each experiment as the mean of these factors from at least five images using the appropriate controls. Typically,  $\alpha = 0.09$ ,  $\beta = 0.08$ , and  $\gamma = 1.8$ . Only molecules that showed single-step donor or acceptor photobleaching were included in the analysis and were curated manually. Mean FRET was calculated by the fitting of one or two gaussians into the histogram of the FRET values aggregated from all time points of all the molecules analysed.

To compare the measured FRET values to FRET estimated from the distances of the dyes attached to the proteins at the indicated positions, we calculated the mean dye accessible volume for each labelled position as described<sup>67</sup>. Briefly, models of the crystal structure of the C<sub>μ</sub>4 (pdb id: 4JVW), crystal structure of the IgG1 (pdb id: 3D03) and Cryo-EM structure of the IgM pentamer (pdb id 6KXS) were used to virtually attach the donor and acceptor dyes to the C<sub>β</sub> atoms of the appropriate residues after the original sidechains had been removed. The accessible dye volume clouds were generated using the FPS software using the settings stated in Supplementary Table 4<sup>67</sup>.

The accessible volume was then used to derive the mean inter-dye distance (FRET-weighted) and the predicted FRET value for each labelling situation, with R<sub>0</sub> for the Alexa Fluor 555 – Alexa Fluor 647 pair set to 5.1 nm.

### Reporting summary

Further information on research design is available in the Nature Research Reporting Summary linked to this article.

### Data availability

The structural data that support the findings of this study have been deposited in the Protein Data Bank and EM Data Bank. The pentameric IgM EM map displayed in Fig. 1 has entry number [EMD-13921](#). The five IgM conformations shown in Fig. 3 are conformation 1 ([EMD-15375](#), [pdb 8ADY](#)), conformation 2 ([EMD-15376](#), [pdb 8ADZ](#)), conformation 3 ([EMD-15377](#), [pdb 8AE0](#)), conformation 4 ([EMD-15380](#), [pdb 8AE3](#)), conformation 5 ([EMD-15379](#), [pdb 8AE2](#)). The monomer IgM-Fc map and model have entry numbers [7QDO](#) and [EMD-13922](#). 43,332 aligned and dose-weighted micrographs have been deposited on EMPIAR (id [EMPIAR-11077](#)). Sample data of single-molecule FRET have been provided for data analysis at Github (<https://github.com/ptolar/single-molecule-FRET-trace-analysis>). Source data are provided with this paper. All the models used in this study (pdb id 6KXS, 4JVU and 2AGJ) are available in PDB and cited in the paper. Source data are provided with this paper.

### Code availability

Custom MATLAB code to analyse single-molecule FRET from time-lapse images is available at Github (<https://github.com/ptolar/single-molecule-FRET-trace-analysis>).

## References

1. Venkitaraman, A. R., Williams, G. T., Dariavach, P. & Neuberger, M. S. The B-cell antigen receptor of the five immunoglobulin classes. *Nature* **352**, 777–781 (1991).
2. Kaetzel, C. S. The polymeric immunoglobulin receptor: Bridging innate and adaptive immune responses at mucosal surfaces. *Immunol. Rev.* **206**, 83–99 (2005).
3. Turula, H. & Wobus, C. E. The role of the polymeric immunoglobulin receptor and secretory immunoglobulins during mucosal infection and immunity. *Viruses* **10**, 237 (2018).
4. Hughey, C. T., Brewer, J. W., Colosia, A. D., Rosse, W. F. & Corley, R. B. Production of IgM hexamers by normal and autoimmune B cells: implications for the physiologic role of hexameric IgM. *J. Immunol.* **161**, 4091–4097 (1998).
5. Mestecky, J., Zikan, J. & Butler, W. T. Immunoglobulin M and secretory immunoglobulin A: Presence of a common polypeptide chain different from light chains. *Science* **171**, 1163–1165 (1971).
6. Halpern, M. S. & Koshland, M. E. Novel subunit in secretory IgA. *Nature* **228**, 1276–1278 (1970).
7. Davis, A. C., Roux, K. H. & Shulman, M. J. On the structure of polymeric IgM\*. *Eur. J. Immunol.* **18**, 1001–1008 (1988).
8. Cook, G. *Immunobiology: The Immune System in Health and Disease (4th edn)* by C. A. Janeway, P. Travers, M. Walport and J. D. Capra. *Immunology Today* **21**, (Elsevier, 2000).
9. Ochsenbein, A. F. et al. Control of early viral and bacterial distribution and disease by natural antibodies. *Science* **286**, 2156–2159 (1999).
10. Boes, M., Prodeus, A. P., Schmidt, T., Carroll, M. C. & Chen, J. A critical role of natural immunoglobulin M in immediate defense against systemic bacterial infection. *J. Exp. Med.* **188**, 2381–2386 (1998).
11. Müller, R. et al. High-resolution structures of the IgM Fc domains reveal principles of its hexamer formation. *PNAS* **110**, 10183–10188 (2013).
12. Hao, G., Wesolowski, J. S., Jiang, X., Lauder, S. & Sood, V. D. Epitope characterization of an anti-PD-L1 antibody using orthogonal approaches. *J. Mol. Recognit.* **28**, 269–276 (2015).
13. Saul, F. A. & Poljak, R. J. Crystal structure of human immunoglobulin fragment Fab new refined at 2.0 Å resolution. *Proteins Struct. Funct. Bioinforma.* **14**, 363–371 (1992).
14. Vyas, N. K. et al. Molecular recognition of oligosaccharide epitopes by a monoclonal Fab specific for *Shigella flexneri* Y lipopolysaccharide: X-ray structures and thermodynamics. *Biochemistry* **41**, 13575–13586 (2002).
15. Tormo, J. et al. Three-dimensional structure of the Fab fragment of a neutralizing antibody to human rhinovirus serotype 2. *Protein Sci.* **1**, 1154–1161 (1992).
16. Mikol, V. Structure of the fab fragment of SDZ CHI621: A chimeric antibody against CD25. *Acta Crystallogr. Sect. D. Biol. Crystallogr.* **52**, 534–542 (1996).
17. Cauerhff, A. et al. Three-Dimensional Structure of the Fab from a Human IgM Cold Agglutinin. *J. Immunol.* **165**, 6422–6428 (2000).
18. Sharp, T. H. et al. Insights into IgM-mediated complement activation based on in situ structures of IgM-C1-C4b. *Proc. Natl Acad. Sci.* **116**, 11900–11905 (2019).
19. Li, Y. et al. Structural insights into immunoglobulin M. *Science* **367**, 1014–1017 (2020).
20. Kumar, N., Arthur, C. P., Ciferri, C. & Matsumoto, M. L. Structure of the human secretory immunoglobulin M core. *Structure* **29**, 1–8 (2021).
21. Vidarsson, G., Dekkers, G. & Rispens, T. IgG subclasses and allotypes: From structure to effector functions. *Front. Immunol.* **5**, 520 (2014).
22. Giuntini, S. et al. Human IgG1, IgG3, and IgG3 Hinge-Truncated Mutants Show Different Protection Capabilities against Meningococci Depending on the Target Antigen and Epitope Specificity. *Clin. Vaccin. Immunol.* **23**, 698–706 (2016).
23. Greer, M. R., Barratt, J., Harper, S. J., Allen, A. C. & Feehally, J. The nucleotide sequence of the IgA1 hinge region in IgA nephropathy. *Nephrol. Dial. Transpl.* **13**, 1980–1983 (1998).
24. Paul, C., Shimizu, A., Kohler, H. & Putnam, F. W. Structure of the Hinge Region of the Mu Heavy Chain of Human IgM Immunoglobulins. *Science* **172**, 69–72 (1971).
25. Seifert, O. et al. The IgM CH2 domain as covalently linked homodimerization module for the generation of fusion proteins with dual specificity. *Protein Eng. Des. Sel.* **25**, 603–612 (2012).
26. Feinstein, A. & Munn, E. A. Conformation of the Free and Antigen-bound IgM Antibody Molecules. *Nature* **224**, 1307–1309 (1969).
27. Hiramoto, E. et al. The IgM pentamer is an asymmetric pentagon with an open groove that binds the AIM protein. *Sci. Adv.* **4**, eaau1199 (2018).
28. Bharathkar, S. K. et al. The structures of secretory and dimeric immunoglobulin A. *Elife* **9**, e56098 (2020).
29. Wang, Y. et al. Structural insights into secretory immunoglobulin A and its interaction with a pneumococcal adhesin. *Cell Res* **30**, 602–609 (2020).
30. Punjani, A. & Fleet, D. J. 3D variability analysis: Resolving continuous flexibility and discrete heterogeneity from single particle cryo-EM. *J. Struct. Biol.* **213**, 107702 (2021).
31. Ramsland, P. A. et al. Crystal structure of a glycosylated Fab from an IgM cryoglobulin with properties of a natural proteolytic antibody. *Biochem. J.* **395**, 473–481 (2006).
32. Ugurlar, D. et al. Structures of C1-IgG1 provide insights into how danger pattern recognition activates complement. *Science* **359**, 794–797 (2018).
33. Lesk, A. M. & Chothia, C. Elbow motion in the immunoglobulins involves a molecular ball-and-socket joint. *Nature* **335**, 188–190 (1988).
34. Roux, K. H., Strelets, L., Brekke, O. H., Sandlie, I. & Michaelsen, T. E. Comparisons of the ability of human IgG3 hinge mutants, IgM, IgE, and IgA2, to form small immune complexes: a role for flexibility and geometry. *J. Immunol.* **161**, 4083–4090 (1998).
35. Zhang, X. et al. 3D Structural Fluctuation of IgG1 Antibody Revealed by Individual Particle Electron Tomography. *Sci. Rep.* **5**, 9803 (2015).
36. Rayner, L. E. et al. The solution structures of two human IgG1 antibodies show conformational stability and accommodate their C1q and FcγR ligands. *J. Biol. Chem.* **290**, 8420–8438 (2015).
37. Keyt, B. A., Baliga, R., Sinclair, A. M., Carroll, S. F. & Peterson, M. S. Structure, Function, and Therapeutic Use of IgM Antibodies. *Antibodies* **9**, 53 (2020).
38. Radaev, S., Motyka, S., Fridman, W. H., Sautes-Fridman, C. & Sun, P. D. The Structure of a Human Type III Fcγ Receptor in Complex with Fc. *J. Biol. Chem.* **276**, 16469–16477 (2001).
39. Herr, A. B., Ballister, E. R. & Bjorkman, P. J. Insights into IgA-mediated immune responses from the crystal structures of human FcαRI and its complex with IgA1-Fc. *Nature* **423**, 614–620 (2003).
40. Wan, T. et al. The crystal structure of IgE Fc reveals an asymmetrically bent conformation. *Nat. Immunol.* **3**, 681–686 (2002).
41. Thies, M. J. W. et al. Folding and association of the antibody domain C(H)3: Prolyl isomerization precedes dimerization. *J. Mol. Biol.* **293**, 67–79 (1999).
42. Benjamin, S. V., Creeke, P. I., Henry, A. J. & McDonnell, J. M. NMR backbone assignment of the Cε4 domain of immunoglobulin E. *Biomol. NMR Assign.* **14**, 151–155 (2020).
43. Giannone, C. et al. Biogenesis of secretory immunoglobulin M requires intermediate non-native disulfide bonds and engagement of the protein disulfide isomerase ERp44. *EMBO J.* **41**, e108518 (2022).

44. Drinkwater, N. et al. Human immunoglobulin E flexes between acutely bent and extended conformations. *Nat. Struct. Mol. Biol.* **21**, 397–404 (2014).
45. Pennington, L. F. et al. Directed evolution of and structural insights into antibody-mediated disruption of a stable receptor-ligand complex. *Nat. Commun.* **12**, 7069 (2021).
46. Oskam, N. et al. At Critically Low Antigen Densities, IgM Hexamers Outcompete Both IgM Pentamers and IgG1 for Human Complement Deposition and Complement-Dependent Cytotoxicity. *J. Immunol.* **209**, 16–25 (2022).
47. Collins, C., Tsui, F. W. L. & Shulman, M. J. Differential activation of human and guinea pig complement by pentameric and hexameric IgM. *Eur. J. Immunol.* **32**, 1802–1810 (2002).
48. Su, Q. et al. Cryo-EM structure of the human IgM B cell receptor. *Science* **377**, 875–880 (2022).
49. Na, X. et al. Cryo-EM structures of two human B cell receptor iso-types. *Science* **377**, 880–885 (2022).
50. Damelang, T., Rogerson, S. J., Kent, S. J. & Chung, A. W. Role of IgG3 in Infectious Diseases. *Trends Immunol.* **40**, 197–211 (2019).
51. Chu, T. H. et al. Hinge length contributes to the phagocytic activity of HIV-specific IgG1 and IgG3 antibodies. *PLoS Pathog.* **16**, e1008083 (2020).
52. Valeich, J. et al. Taking the Hinge off: An Approach to Effector-Less Monoclonal Antibodies. *Antibodies* **9**, 50 (2020).
53. Dong, H. & Hartgerink, J. D. Short homodimeric and heterodimeric coiled coils. *Biomacromolecules* **7**, 691–695 (2006).
54. Zheng, S. Q. et al. MotionCor2: Anisotropic correction of beam-induced motion for improved cryo-electron microscopy. *Nat. Methods.* **14**, 331–332 (2017).
55. Rohou, A. & Grigorieff, N. CTFIND4: Fast and accurate defocus estimation from electron micrographs. *J. Struct. Biol.* **192**, 216–221 (2015).
56. Wagner, T. et al. SPHIRE-crYOLO is a fast and accurate fully automated particle picker for cryo-EM. *Commun. Biol.* **2**, 218 (2019).
57. Punjani, A., Rubinstein, J. L., Fleet, D. J. & Brubaker, M. A. cryoSPARC: algorithms for rapid unsupervised cryo-EM structure determination. *Nat. Methods.* **14**, 290–296 (2017).
58. Punjani, A., Zhang, H. & Fleet, D. J. Non-uniform refinement: adaptive regularization improves single-particle cryo-EM reconstruction. *Nat. Methods.* **17**, 1214–1221 (2020).
59. Afonine, P. V. et al. New tools for the analysis and validation of cryo-EM maps and atomic models. *Acta Crystallogr. Sect. D. Struct. Biol.* **D74**, 814–840 (2018).
60. Pettersen, E. F. et al. UCSF Chimera - A visualization system for exploratory research and analysis. *J. Comput. Chem.* **25**, 1605–1612 (2004).
61. Zivanov, J. et al. New tools for automated high-resolution cryo-EM structure determination in RELION-3. *Elife* **7**, e42166 (2018).
62. Zivanov, J., Nakane, T. & Scheres, S. H. W. A Bayesian approach to beam-induced motion correction in cryo-EM single-particle analysis. *IUCrJ.* **6**, 5–17 (2019).
63. Schneider, C. A., Rasband, W. S. & Eliceiri, K. W. NIH Image to ImageJ: 25 years of Image Analysis. *Nat. Methods.* **9**, 671–675 (2012).
64. Rudich, S. M., Mihaesco, E., Winchester, R. & Mongini, P. K. Analysis of the domain specificity of various murine anti-human IgM monoclonal antibodies differing in human B lymphocyte signaling activity. *Mol. Immunol.* **24**, 809–820 (1987).
65. McCann, J. J., Choi, U. B., Zheng, L., Weninger, K. & Bowen, M. E. Optimizing methods to recover absolute FRET efficiency from immobilized single molecules. *Biophys. J.* **99**, 961–970 (2010).
66. Roy, R., Hohng, S. & Ha, T. A practical guide to single-molecule FRET. *Nat. Methods.* **5**, 507–516 (2008).
67. Kalinin, S. et al. A toolkit and benchmark study for FRET-restrained high-precision structural modeling. *Nat. Methods.* **9**, 1218–1225 (2012).

## Acknowledgements

We thank A. Nans of the Structural Biology Science Technology Platform for assistance with data collection and computing; P. Walker and A. Purkiss of the Structural Biology Science Technology Platform; G. Mashanov and J. Molloy for help with single-molecule FRET set-up; the Scientific Computing Science Technology Platform for computational support. This work was supported by the Francis Crick Institute, which receives its core funding from Cancer Research UK (FC001143 (P.B.R), FC001185 (P.T.)), the UK Medical Research Council (FC001143 (P.B.R), FC001185 (P.T.)), and the Wellcome Trust (FC001143 (P.B.R), FC001185 (P.T.)).

## Author contributions

Q.C., R.M. and L.C. performed experiments. Q.C., R.M., L.C., P.T., and P.B.R. contributed to experimental design, data analysis and manuscript writing.

## Funding

Open Access funding provided by The Francis Crick Institute.

## Competing interests

The authors declare no competing interests.

## Additional information

**Supplementary information** The online version contains supplementary material available at <https://doi.org/10.1038/s41467-022-34090-2>.

**Correspondence and requests** for materials should be addressed to Pavel Tolar or Peter B. Rosenthal.

**Peer review information** *Nature Communications* thanks Roberto Sitia and the other, anonymous, reviewer(s) for their contribution to the peer review of this work.

**Reprints and permissions information** is available at <http://www.nature.com/reprints>

**Publisher's note** Springer Nature remains neutral with regard to jurisdictional claims in published maps and institutional affiliations.

**Open Access** This article is licensed under a Creative Commons Attribution 4.0 International License, which permits use, sharing, adaptation, distribution and reproduction in any medium or format, as long as you give appropriate credit to the original author(s) and the source, provide a link to the Creative Commons license, and indicate if changes were made. The images or other third party material in this article are included in the article's Creative Commons license, unless indicated otherwise in a credit line to the material. If material is not included in the article's Creative Commons license and your intended use is not permitted by statutory regulation or exceeds the permitted use, you will need to obtain permission directly from the copyright holder. To view a copy of this license, visit <http://creativecommons.org/licenses/by/4.0/>.

© The Author(s) 2022